

Kiloparsec-scale radio emission in Seyfert and LINER galaxies

Veeresh Singh^{1,2,3*}, C. H. Ishwara-Chandra¹, Yogesh Wadadekar¹, Alexandre Beelen² and Preeti Kharb⁴

¹National Centre for Radio Astrophysics, TIFR, Post Bag 3, Ganeshkhind, Pune 411007, India

²Institut d'Astrophysique Spatiale, Bât. 121, Université Paris-Sud, 91405 Orsay Cedex, France

³Astrophysics and Cosmology Research Unit, School of Chemistry and Physics, University of KwaZulu-Natal, Durban 4041, South Africa

⁴Indian Institute of Astrophysics, Bangalore 560034, India

Accepted; Received; in original form

ABSTRACT

Seyfert and LINER galaxies are known to exhibit compact radio emission on ~ 10 to 100 parsec scales, but larger Kiloparsec-Scale Radio structures (KSRs) often remain undetected in sub-arcsec high resolution observations. We investigate the prevalence and nature of KSRs in Seyfert and LINER galaxies using the 1.4 GHz VLA FIRST and NVSS observations. Our sample consists of 2651 sources detected in FIRST and of these 1737 sources also have NVSS counterparts. Considering the ratio of total to peak flux density ($\theta = (S_{\text{int}}/S_{\text{peak}})^{1/2}$) as a parameter to infer the presence of extended radio emission we show that $\geq 30\%$ of FIRST detected sources possess extended radio structures on scales larger than 1.0 kpc. The use of low-resolution NVSS observations help us to recover faint extended KSRs that are resolved out in FIRST observations and results in $\geq 42.5\%$ KSR sources in FIRST–NVSS subsample. This fraction is only a lower limit owing to the combination of projection, resolution and sensitivity effects. Our study demonstrates that KSRs may be more common than previously thought and are found across all redshifts, luminosities and radio-loudness. The extranuclear radio luminosity of KSR sources is found to be positively correlated with the core radio luminosity as well as the [O III] $\lambda 5007\text{\AA}$ line luminosity and this can be interpreted as KSRs being powered by AGN rather than star-formation. The distributions of the FIR-to-radio ratios and mid-IR colors of KSR sources are also consistent with their AGN origin. However, contribution from star-formation cannot be ruled out particularly in sources with low radio luminosities.

Key words: galaxies: active, galaxies: Seyfert, radio continuum: galaxies

1 INTRODUCTION

Active Galactic Nuclei (AGN) are classified into radio-loud and radio-quiet subclasses based on the ratio of 5 GHz radio flux density to 4400Å optical continuum flux ($R = \frac{\nu_{5\text{GHz}} S_{5\text{GHz}}}{\nu_{4400\text{\AA}} S_{4400\text{\AA}}}$) with $R \geq 10$ for radio-loud AGN and $R < 10$ for radio-quiet AGN (Kellermann et al. 1989). This dichotomy may also be manifested in radio morphologies as radio-loud AGN exhibit bipolar jets terminating into radio lobes with total end-to-end size spanning upto few hundred kiloparsec to even few Megaparsec. While, radio-quiet AGN often display compact nuclear radio emission with occasional presence of extended radio emission limited to ≤ 10 kiloparsec scale. Seyfert and Low Ionization Nuclear Emission Region (LINER) galaxies are classified as radio-quiet AGN with low optical luminosity ($M_{\text{B-Band}} > -22.25$ assuming $H_0 = 71 \text{ km}$

$\text{s}^{-1} \text{ Mpc}^{-1}$) (Schmidt & Green 1983). High resolution radio observations show that most of the Seyfert galaxies possess compact sub-parsec scale nuclear emission with brightness temperature $\geq 10^7 \text{ K}$ (Thean et al. 2000; Middelberg et al. 2004; Lal et al. 2004). However, radio observations of arcsec resolution have revealed resolved structures, with hints of jets and extended emission in several Seyfert galaxies (Baum et al. 1993; Colbert et al. 1996; Morganti et al. 1999; Gallimore et al. 2006). This is further supported by the examples of few individual Seyfert galaxies that exhibit radio morphology consisting of a core, collimated jets and lobes similar to those found in radio-loud AGN (e.g., NGC 1052 (Wrobel 1984), NGC 1068 (Ulvestad et al. 1987), NGC 7674 (Momjian et al. 2003), MRK 3 (Kukula et al. 1999) and MRK 6 (Kharb et al. 2006)), although, unlike radio-loud AGN the linear radio structures in Seyfert galaxies span only upto few kiloparsec. Also, Kpc-Scale Radio structures (KSRs) in Seyfert galaxies are not always found to be aligned with the pc-scale jet-like structures

* E-mail: Singhv4@ukzn.ac.za

(Colbert et al. 1996; Kharb et al. 2006, 2010). It is believed that the low-power radio jets seen in Seyfert galaxies are analogous to the larger jets seen in radio galaxies but perhaps distorted or stunted by the interaction with the surrounding inter-stellar medium (ISM) of the host galaxy (Whittle & Wilson 2004; Gallimore et al. 2006). Overall it appears that the radio structures in Seyfert galaxies are much more complex than in powerful radio-loud AGN.

It is important to note that most of the radio studies of Seyfert/LINER samples have been carried out mainly at higher frequencies with long-baseline interferometers (*e.g.*, VLA A-array, MERLIN, VLBI) that filter out low-surface-brightness emission distributed over larger angular scales (*e.g.*, Ulvestad & Wilson 1989; Kukula et al. 1995; Thean et al. 2000; Ho & Ulvestad 2001; Lal et al. 2004; Nagar et al. 2005; Panessa & Giroletti 2013). Therefore, high resolution observations are likely to miss the detection of KSRs. Indeed, in some Seyfert galaxies, the radio flux density arising from their parsec-scale structure is found to be much lower than that derived from observations with lower resolution, even if the nucleus appears unresolved. The missing flux has been interpreted as due to the presence of KSRs of low-surface-brightness (Sadler et al. 1995; Orienti & Prieto 2010). In fact, sensitive radio observations of arcsec resolution have suggested that there may be a large fraction of Seyferts with KSRs (*e.g.*, Baum et al. 1993; Kukula et al. 1996; Gallimore et al. 2006). Using deep VLA ‘D’ array observations ($\sim 15 - 20$ arcsec resolution at 5 GHz with average rms $\sim 50 \mu\text{Jy}$) Gallimore et al. (2006) showed that $\geq 44\%$ sources in their sample of 43 Seyfert and LINER galaxies exhibit extended radio structures at least 1 kpc in total extent that do not match the morphology of the disk or its associated star-forming regions. This favors a scenario in which KSRs are likely to be an extension of the nuclear radio jet and therefore related to AGN activity. However, starburst galaxies (*e.g.*, M82 (Seaquist & Odegard 1991) and NGC 253 (Carilli et al. 1992)) are also known to display KSRs probably originating from a superwind generated by the cumulative effects of stellar winds. These results raise questions whether KSRs are truly so common in Seyfert and LINER galaxies and whether they are related to the AGN or starburst. We note that all the previous studies on KSRs are limited to targeted observations of fairly small samples despite the availability of large Seyfert/LINER samples. In order to detect and examine the prevalence and nature of KSRs in Seyfert and LINER galaxies we study radio emission properties in a large sample of ~ 2651 sources using 1.4 GHz VLA FIRST and NVSS radio surveys. Our sample of Seyfert and LINER galaxies is derived from the 13th edition AGN catalog of Véron-Cetty & Véron (2010) and is the largest sample of Seyfert and LINER galaxies hitherto used for KSRs studies.

This paper is organized as follows. In Section 2, we discuss our sample selection and its merits. The details on the radio data are given in Section 3 and the identification of FIRST and NVSS radio counterparts is discussed in Section 4. The methods of using flux densities to ascertain the presence of extended emission are discussed in Section 5. A brief discussion on the sources with multicomponent radio structures is presented in Section 6. Section 7 is devoted to the discussion on the origin of KSRs. The conclusions of our study are given in Section 8.

In this paper we have assumed $H_0 = 71 \text{ km s}^{-1} \text{ Mpc}^{-1}$, $\Omega_M = 0.27$, $\Omega_\Lambda = 0.73$.

Table 1. Number of Seyferts and LINERs detected in FIRST and NVSS

| Class | S1 | S2 | S3 |
|--|-------|------|-----|
| No. of sources in VV10 catalog | 16517 | 6024 | 907 |
| No. of sources detected in FIRST | 1373 | 1164 | 114 |
| No. of sources detected in both FIRST and NVSS | 884 | 753 | 100 |

2 THE SAMPLE

Our sample of Seyfert and LINER galaxies is derived from the 13th edition AGN catalog of Véron-Cetty & Véron (2010) (hereafter VV10) which is the most updated complete survey of the literature and lists all the quasars, BL Lacs, active galaxies known to the catalog authors prior to July 1, 2009. The VV10 catalog follows conventional definition of Seyfert and LINER galaxies that are defined as AGN of low optical luminosity with absolute B-band magnitude fainter than -22.25 (*i.e.*, $M_B > -22.25$) (Schmidt & Green 1983). The use of Hubble parameter $H_0 = 71 \text{ km s}^{-1} \text{ Mpc}^{-1}$ instead of $50 \text{ km s}^{-1} \text{ Mpc}^{-1}$ has changed the optical luminosity limit to $M_B = -22.25$ rather than $M_B = -23.0$ considered in some early studies. The VV10 catalog contains total 34231 Low Luminosity AGN (LLAGN) with $M_B > -22.25$. To select our sample of Seyfert and LINER galaxies we have taken only those sources that have confirmed Seyfert or LINER classification in the VV10 catalog and excluded sources without classification or with uncertain classification. We refer Seyfert and LINER galaxies collectively as ‘LLAGN’. We obtain a sample of 23448 LLAGN that contains 16517 Seyfert 1s (designated as ‘S1’), 6024 Seyfert 2s (designated as ‘S2’), and 907 LINERs (designated as ‘S3’). In our sample we have grouped intermediate Seyferts (*i.e.*, types 1.0, 1.2, 1.5, 1.8, and 1.9) into Seyfert type 1s noting the fact that intermediate Seyferts are classified based on the appearance of broad permitted Balmer lines which are characteristics of type 1s (Osterbrock 1981). Narrow line Seyfert galaxies (designated as ‘S1n’) and Seyfert galaxies with broad permitted lines detected in infrared wavelengths (designated as ‘S1i’) or in polarized light (designated as ‘S1h’) are also included in Seyfert type 1s.

Table 1 lists the number of Seyferts and LINERs extracted from the VV10 catalog and their detections in FIRST and NVSS radio surveys. Figure 1 shows the redshift distributions of all Seyfert and LINER galaxies detected in FIRST survey. The FIRST detected LLAGN have median redshift (z_{median}) ~ 0.15 , with 98.7% at $z \leq 1.0$. In comparison to Seyfert galaxies, LINERs are seen at lower redshifts with median redshift (z_{median}) ~ 0.048 . The FIRST detected Seyfert type 1s and type 2s have similar redshift distributions with median redshifts ~ 0.158 and ~ 0.162 , respectively. Two sample Kolmogorov-Smirnov (KS) test shows that the redshift distributions of Seyfert 1s and Seyfert 2s are similar ($D \sim 0.05$) with probability of null hypothesis that the two samples are drawn from two different parent population is only 0.095. Since our final sample consists of FIRST detected sources (*i.e.*, radio selected) and radio emission is optically thin to dust obscuration, therefore, our sample is unaffected by the biases introduced by obscuration caused by dusty torus present around AGN. This is evident from the comparison of redshift distributions of Seyfert type 1s and type 2s. In general, optically selected Seyfert samples are known to be biased against Seyfert type 2s as AGN view is intercepted by the circumnuclear obscuring torus (Ho & Ulvestad 2001).

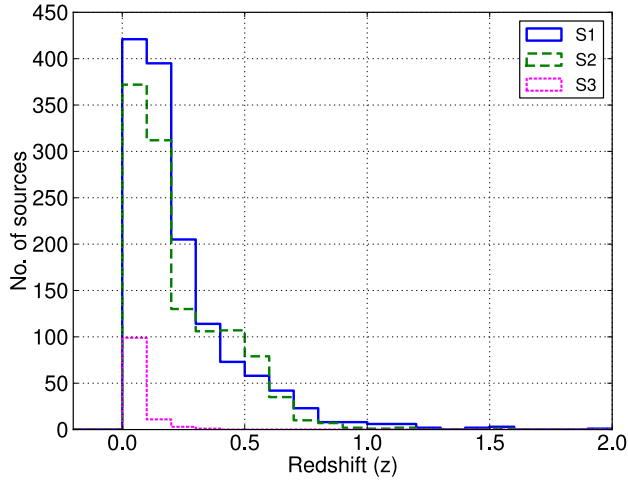


Figure 1. Redshift distributions of Seyfert 1s, Seyfert 2s and LINERs (S3) detected in FIRST.

3 RADIO DATA

We use the “*Faint Images of the Radio Sky at Twenty-cm*” (FIRST¹) survey carried out at 1.4 GHz by Very Large Array (VLA) in its B-configuration and it covers sky region over 10,000 square degrees of the North and South Galactic Caps (Becker et al. 1995). The FIRST radio maps have resolution of $\sim 5''$ and typical rms down to ~ 0.15 mJy. We have used most recent version of FIRST source catalog (released on March 2014) that lists peak as well as integrated flux densities and radio sizes derived by fitting a two-dimensional Gaussian to a source detected at a flux limit of ~ 1.0 mJy ($\text{SNR} \geq 5.0$). The astrometric reference frame of FIRST maps is accurate to $\sim 0.05''$ and individual sources have $\sim 90\%$ confidence error circles of radius $< 0.5''$ at the 3 mJy level and $\sim 1''$ at the survey threshold.

In order to detect faint kpc-scale extended radio emission we also use the “*NRAO VLA Sky Survey*” (NVSS²) which is a 1.4 GHz continuum survey carried out by VLA in its ‘D’ configuration. NVSS covers the entire sky north of -40° declination and produces radio images with resolution of $\sim 45''$ and sensitivity of ~ 2.4 mJy at 5σ level (Condon et al. 1998). NVSS observations of low resolution are advantageous in detecting low-surface-brightness KSRs that are resolved out, and therefore, missed by higher resolution FIRST observations. We use the NVSS catalog which contains over 1.8 million unique detections brighter than 2.5 mJy and give total integrated 1.4 GHz flux densities of all the radio sources. The astrometric accuracy ranges from $\sim 1''.0$ for the brightest NVSS detections to about $\sim 7''.0$ for the faintest detections.

4 FIRST AND NVSS RADIO COUNTERPARTS

4.1 FIRST counterparts of Seyfert and LINER galaxies

To find the radio counterparts of Seyfert and LINER galaxies in FIRST survey we searched for FIRST detection around the optical positions of sources. The accurate astrometry of FIRST and optical

positions of LLAGN allows us to use a simple positional matching with high completeness and low contamination. The source positions in the FIRST as well as in the VV10 catalog are measured with an accuracy better than one arcsec (Becker et al. 1995; Véron-Cetty & Véron 2010). The choice of matching radius between the optical and radio positions is a trade off between the completeness and contamination, *i.e.*, a smaller matching radius greatly reduces the contamination at the expense of completeness. In order to choose an optimum matching radius, we cross-matched our LLAGN to the FIRST sources using a large matching radius of 30 arcsec and plotted the histogram of the separation between the LLAGN optical position and FIRST radio position for all the cross-match sources. We find that the histogram follows nearly a Gaussian distribution between 0 to 3.0 arcsec and a flat tail on-wards (see Figure 2). Therefore, based on the histogram of the separation between LLAGN optical positions and FIRST radio positions, we choose matching radius to be 3.0 arcsec. Previous studies on the cross-matching between Seyfert galaxies and the FIRST sources have also reported 3.0 arcsec as a reliable limit with negligible probability ($< 0.05\%$) of being merely a chance match (see Wadadekar 2004).

The cross-matching of our LLAGN sample sources and the FIRST sources using a matching radius of 3.0 arcsec results in 2651 sources. Table 1 lists the number of Seyfert type 1s, Seyfert type 2s and LINER galaxies detected in FIRST. Before cross-matching LLAGN and FIRST sources we corrected for systematic offset between optical and radio catalogs (*i.e.*, $\Delta\text{RA} = \text{RA}_{\text{LLAGN}} - \text{RA}_{\text{FIRST}} = -0.025$ arcsec and $\Delta\text{DEC} = \text{DEC}_{\text{LLAGN}} - \text{DEC}_{\text{FIRST}} = -0.31$ arcsec). Also, in cross-matching we considered only those FIRST sources that have sidelobe probability ≤ 0.1 (*i.e.*, there is 90% probability that the FIRST source is real). To check the level of contamination by chance matching in our cross-matched sample we shifted the optical positions of our LLAGN by 30 to 45 arcsec in random directions and find only 0.3% cross-matched sources. This shows that the contamination due to chance matching in our cross-matched sample is negligible.

To find extended radio sources with multicomponents, we searched for radio components around all the 2651 FIRST detected LLAGN using a large search radius of 120 arcsec. We made visual inspection of the FIRST cutout images of all the sources that show one or more radio components within 120 arcsec around the central core radio component. We exclude radio components that are completely unrelated to the source. This exercise resulted in a total of 180 out of 2651 LLAGN that having multicomponents detected in the FIRST survey. To get the total flux density of a source with multicomponents, we add up integrated flux densities of all the components. We note that, in general, extended radio morphologies of Seyfert and LINER galaxies are more complex and diverse than core-jet-lobe morphology seen in radio galaxies. Therefore, to search for extended sources with multicomponents, it is not possible to opt for a single criterion that are often being used for quasars *i.e.*, two radio sources are located nearly symmetrically around the quasar position and the ratio of their distances to the quasar is $1/3 < d_1/d_2 < 3$ (de Vries et al. 2006). In fact, even for quasars with more complex radio morphologies (*i.e.*, sources with distorted asymmetric lobes and a compact core, or for cases in which extended lobes are resolved into complex structure), the visual inspection needs to be used (see Lu et al. 2007).

¹ <http://sundog.stsci.edu/>

² <http://www.cv.nrao.edu/nvss/>

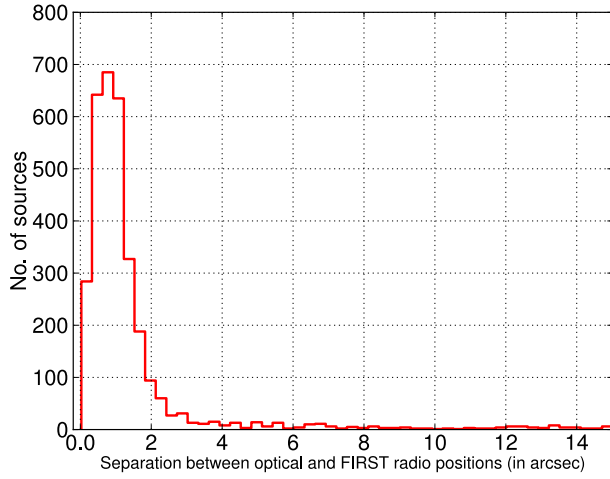


Figure 2. Histogram of the separation between optical and FIRST radio positions of the cross-matched sources of LLAGN from VV10 and FIRST catalog.

4.2 NVSS counterparts of FIRST-detected Seyfert and LINER galaxies

To find the NVSS counterparts of FIRST detected LLAGN we use a search radius of 20 arcsec for all the sources that show only a single component in the FIRST. The histogram of the separation between FIRST and NVSS positions of cross-matched sources tails off beyond 20 arcsec (see Figure 3). Using a matching radius larger than 20 arcsec (*e.g.*, 30 to 45 arcsec) gives only 1% to 2% increase in the number of cross-matched sources which is comparable to the level of chance matching. Thus, we chose optimum matching radius to 20 arcsec at which chance matching is only 0.9% (*i.e.*, with FIRST source density $\sim 90 \text{ deg}^{-2}$). For extended sources with multicomponents in FIRST, we use matching radius equal to the separation between two farthest components and obtain NVSS counterparts of all such sources. We made visual inspection of FIRST and NVSS image cutouts to ensure reliable cross-matching. The cross-matching between our FIRST detected LLAGN and NVSS catalog yields NVSS counterparts for 1737 out of 2651 sources (*i.e.*, 65.5%). Most of FIRST detected LLAGN that remained undetected in NVSS fall below the NVSS flux limit *i.e.*, 2.5 mJy. Table in the appendix lists the FIRST and NVSS parameters of our sample sources.

5 FLUX DENSITY RATIO DIAGNOSTIC TO IDENTIFY EXTENDED RADIO EMISSION

We can classify a radio source as unresolved or resolved by defining a dimensionless concentration parameter $\theta = (S_{\text{int}}/S_{\text{peak}})^{1/2}$ (Ivezic et al. 2002). Using the distribution of radio sources in the two-dimensional plot of θ versus extended flux density, Kimball & Ivezić (2008) proposed that FIRST radio sources can be categorized as ‘unresolved’ and ‘resolved’ by defining $\theta = (S_{\text{int, FIRST}}/S_{\text{peak, FIRST}})^{1/2} \approx 1.06$ as a separating value. Therefore, we use the parameter $\theta = (S_{\text{int}}/S_{\text{peak}})^{1/2}$ (square root of the ratio of integrated to peak flux density of FIRST) to infer the presence of extended radio emission at scale larger than the FIRST beam-size of ~ 5 arcsec.

Furthermore, FIRST is a relatively high-resolution radio survey,

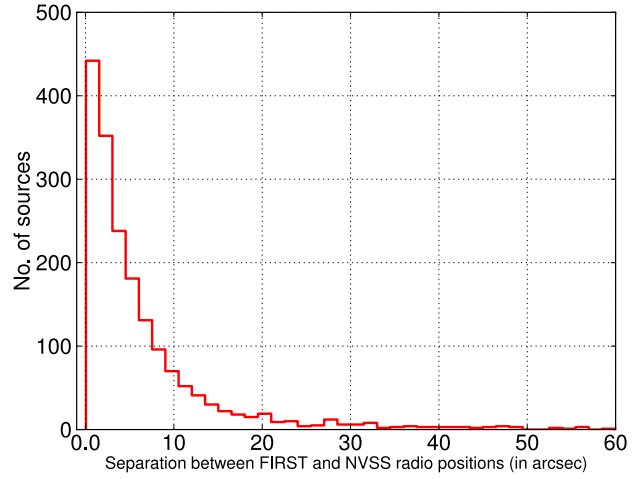


Figure 3. Histogram of the separation between FIRST and NVSS radio positions.

and therefore, underestimates the flux of extended and lobe-dominated sources (Becker et al. 1995; Lu et al. 2007). Also, multiple-component radio sources with core and lobes are often detected as separate objects by FIRST but as only a single object in the lower-resolution NVSS observations at same wavelength. Therefore, the ratio between the NVSS and FIRST flux densities can be used as a diagnostic measure of the presence of faint extended radio emission that is missed by FIRST. Kimball & Ivezić (2008) showed that the distribution of the difference of FIRST and NVSS radio magnitudes $\Delta t = t_{\text{FIRST}} - t_{\text{NVSS}}$ is bimodal with two peaks centered at $\Delta t = 0$ and $\Delta t = 0.7$; where radio magnitude is defined as $t = -2.5 \log(\frac{S_{\text{int}}}{3631 \text{ Jy}})$. The visual inspection of thousand of FIRST images confirmed that sources at the $\Delta t = 0$ locus are single component sources, while those in the $\Delta t = 0.7$ locus are multiple-component or extended. By fitting the bimodal distribution of Δt with two Gaussians Kimball & Ivezić (2008) proposed that $\Delta t = t_{\text{FIRST}} - t_{\text{NVSS}} \approx 0.35$ can be used as a separating value between ‘simple’ ($\Delta t < 0.35$) and ‘complex’ ($\Delta t > 0.35$) radio morphologies. In terms of flux density ratio, the difference in FIRST and NVSS radio magnitude $\Delta t = 0.35$ corresponds to $\frac{S_{\text{int, NVSS}}}{S_{\text{int, FIRST}}} \approx 1.38$. Hence, we define a parameter $\theta_{\text{NVSS-FIRST}} = (S_{\text{NVSS, int}}/S_{\text{FIRST, int}})^{1/2}$ with separating value $\theta_{\text{NVSS-FIRST}} = 1.175$ (*i.e.*, corresponding $\Delta t = 0.35$) to classify radio sources into ‘simple’ ($\theta_{\text{NVSS-FIRST}} \leq 1.175$) and ‘complex’ ($\theta_{\text{NVSS-FIRST}} > 1.175$) radio morphology categories.

Therefore, using FIRST and NVSS flux densities we can divide radio sources into following classes.

- (i) ‘Unresolved’ point sources in FIRST with ‘simple’ radio morphology inferred from FIRST-NVSS flux density comparison. These sources can be characterized with $\theta_{\text{FIRST}} \leq 1.06$ and $\theta_{\text{NVSS-FIRST}} \leq 1.175$.
- (ii) ‘Unresolved’ sources in FIRST but with ‘complex’ radio morphology inferred from FIRST-NVSS flux density comparison. These sources can be characterized with $\theta_{\text{FIRST}} \leq 1.06$ and $\theta_{\text{NVSS-FIRST}} > 1.175$. These sources possess extended low-surface-brightness radio emission that is resolved out in FIRST but detected in NVSS due to larger beam-size.
- (iii) ‘Resolved’ sources in FIRST but ‘simple’ radio morphology inferred from FIRST-NVSS flux density comparison. These sources can be characterized with $\theta_{\text{FIRST}} > 1.06$ and $\theta_{\text{NVSS-FIRST}} \leq$

1.175. These sources do have extended radio emission detected in FIRST but there is no significant additional flux detected by NVSS. (iv) ‘Resolved’ sources in FIRST and ‘complex’ radio morphology inferred from FIRST-NVSS comparison. These sources can be characterized with $\theta_{\text{FIRST}} > 1.06$ and $\theta_{\text{NVSS-FIRST}} > 1.175$. These sources do have extended radio emission detected in FIRST and also have additional faint low-surface-brightness radio emission component detected in NVSS.

In interpreting the results based on the flux density ratios we should keep the caveat in mind that FIRST has higher sensitivity than NVSS. Table 2 lists the number and fraction of Seyferts/LINER galaxies with unresolved/resolved and simple/complex radio morphologies.

5.1 Comparison of total to peak flux densities in FIRST

Figure 4 (left panel) shows the distribution of FIRST total flux density ($S_{\text{int,FIRST}}$) versus $\theta_{\text{FIRST}} = (S_{\text{int,FIRST}}/S_{\text{peak,FIRST}})^{1/2}$. It is evident that resolved sources with extended radio emission larger than $5''$ (*i.e.*, $\theta_{\text{FIRST}} > 1.06$) are present across all flux densities. Although, sources with high ratios of total-to-peak flux densities are found only in radio bright LLAGN. For example, sources with $\theta_{\text{FIRST}} > 2.0$ (*i.e.*, S_{int} higher than 4 times of S_{peak}) are found only at $S_{\text{int}} \geq 5.0$ mJy. The comparison of FIRST total to peak density (θ_{FIRST}) shows that $827/2615 \sim 31.2\%$ sources possess extended radio emission on scales larger than 5 arcsec (see Table 2). We note that the resolved sources with extended radio emission ($\theta_{\text{FIRST}} > 1.06$) are distributed across all redshifts spanning over 0.002 to 2.26 with median redshift ~ 0.136 (figure 4, right panel). There are $794/2651 \sim 30\%$ sources with redshift (z) ≥ 0.01 , where 5 arcsec angular size corresponds to ≥ 1.0 kpc. Therefore, we infer that 30% FIRST detected LLAGN possess KSRs *i.e.*, radio emitting structures larger than 1.0 kpc. This is only a lower limit as sources with radio structures of ≥ 1.0 kpc would appear unresolved at higher redshifts ($z \geq 0.01$). Also, LLAGN with AGN-jet lying close to the line-of-sight (in type 1s) would have much smaller projected size and therefore, would appear as unresolved despite possessing extended radio emission.

5.2 Comparison of NVSS and FIRST flux densities

The faint extended low-surface-brightness radio emission that is resolved out in FIRST observations can be detected in NVSS due to its much larger $45''$ beam. Therefore, we also compare NVSS and FIRST total flux densities by defining a parameter $\theta_{\text{NVSS-FIRST}} = (S_{\text{int,NVSS}}/S_{\text{int,FIRST}})^{1/2}$ which is used to infer the radio morphologies of our sample sources. Figure 5 (Left panel) shows the distribution of FIRST total flux density ($S_{\text{int,FIRST}}$) versus $\theta_{\text{NVSS-FIRST}} = (S_{\text{int,NVSS}}/S_{\text{int,FIRST}})^{1/2}$. It is clear that sources characterized with complex morphology (*i.e.*, $\theta_{\text{NVSS-FIRST}} > 1.75$) are present in radio faint as well as in radio bright LLAGN. However, there is no additional NVSS flux density detected in very bright radio sources *i.e.*, $S_{\text{int,FIRST}} \geq 100$ mJy. Table 2 lists the number and fraction of LLAGN that possess additional flux density detected in NVSS but missed out in FIRST. We note that the extra flux detected in NVSS is present in resolved as well as unresolved FIRST sources. The comparison of NVSS and FIRST flux densities reveals the presence of complex radio morphology (*i.e.*, $\theta_{\text{NVSS-FIRST}} > 1.75$) in $\sim 17\%$ of FIRST-NVSS detected sources. Interestingly, there are $\sim 11\%$ FIRST-NVSS detected LLAGN in which FIRST detects only unresolved compact emission ($\theta_{\text{FIRST}} < 1.06$) while NVSS picks up additional flux density ($\theta_{\text{FIRST}} > 1.175$). Thus, in $\sim 11\%$ of

sources, the comparison of NVSS and FIRST flux densities helps to recover low-surface-brightness extended radio emission that is missed in FIRST observations. Total fraction of sources with extended radio emission identified either via FIRST (θ_{FIRST}) or via NVSS ($\theta_{\text{NVSS-FIRST}}$) flux diagnostics is as high as $\sim 45\%$ among the FIRST-NVSS detected LLAGN (see Table 2). The $\theta_{\text{NVSS-FIRST}}$ versus redshift (z) plot (see Figure 5; right panel) shows that complex sources are present across all redshifts. Among the FIRST-NVSS detected LLAGN there are $911/1737 \sim 42\%$ resolved/complex sources lying at redshift $z \geq 0.01$ and thus possess KSRs (*i.e.*, $5''$ angular scale corresponds to 1.0 kpc at $z \geq 0.01$). We note that this fraction is only a lower limit as it is possible that in sources of bright compact component with very faint extended emission, the total flux is primarily due to the brighter compact component, thus, resulting $\theta_{\text{NVSS-FIRST}} = (S_{\text{int,NVSS}}/S_{\text{int,FIRST}})^{1/2} \leq 1.06$ with source being classified as compact.

Figure 6 shows θ_{FIRST} versus $\theta_{\text{NVSS-FIRST}}$ plot. This plot does not show any systematic trend suggesting that there are wide variety of radio sources *i.e.*, (i) unresolved sources in both FIRST and NVSS, (ii) unresolved sources in FIRST but extended emission detected in NVSS, (iii) resolved sources in FIRST with no extra flux density in NVSS, and (iv) resolved sources in FIRST with additional flux density detected in NVSS. Indeed, this is also evident from table 2 that lists the fraction of sources with different radio morphologies.

Table 3 shows the comparison of the fraction of KSR sources in our sample and previous studies. It is evident that high-resolution radio observations carried out at higher frequencies miss the detection of KSRs. While low-frequency observations with relatively lower resolution can efficiently detect kpc-scale radio emission of low-surface-brightness. Noting the importance of low-frequency observations with relatively low-resolution in detecting KSRs, we have carried out 325 MHz and 610 MHz Giant Metrewave Radio Telescope (GMRT) observations of a carefully chosen sample of Seyfert galaxies (*e.g.*, Kharb et al. 2014). Our investigation on faint KSRs using low-frequency GMRT observations is expected to conclude soon (Singh et al. 2015, in progress).

6 LLAGN WITH MULTICOMPONENT RADIO EMISSION DETECTED IN FIRST

There are a total of 180 Seyfert and LINER galaxies in our sample that display multicomponent radio emission in FIRST observations. These sources have more than one components wherein each component is fitted with an elliptical Gaussian. In figure 7, we show FIRST and NVSS contours overplotted on the DSS optical images for three sources (*i.e.*, NGC 4636, NGC 5033 and NGC 7479) that display extended multicomponent radio emission.

(i) FIRST observations of NGC 4636, a LINER galaxy at redshift (z) ~ 0.003 , show an S-shaped radio structure with projected size of ~ 2.48 kpc (~ 40 arcsec) along Position Angle (PA) $\sim 40^\circ$ (see Figure 7, left panel). There is another radio component located at the distance of $\sim 34''$ to the west of the central component. The jet-like radio structure accompanied by a strong ridge of radio emission displaying an S-shaped structure of ~ 5.0 kpc has been reported in previous observations (see Birkinshaw & Davies 1985). The linear jet-like radio structure lies nearly along the minor axis of host galaxy (Stanger & Warwick 1986).

(ii) The FIRST image of NGC 5033, a Seyfert type 1.8 galaxy at redshift (z) ~ 0.003 , shows a central radio component accompanied by a diffuse extended radio structures with projected size of

Table 2. Radio morphology

| Radio morphology | θ_{FIRST} | $\theta_{\text{NVSS-FIRST}}$ | All | No. of sources | | |
|-------------------------------|-------------------------|------------------------------|--------------|----------------|-------------|------------|
| | | | | S1 | S2 | S3 |
| <i>FIRST detected sources</i> | | | 2651 | 1373 | 1164 | 114 |
| Unresolved | ≤ 1.06 | | 1824 (68.8%) | 913 (66.5%) | 839 (72.1%) | 72 (63.2%) |
| Resolved | > 1.06 | | 827 (31.2%) | 460 (33.5%) | 325 (27.9%) | 42 (36.8%) |
| <i>FIRST - NVSS pair</i> | | | 1737 | 884 | 753 | 100 |
| Unresolved and simple | ≤ 1.06 | ≤ 1.175 | 961 (55.3%) | 463 (52.4%) | 447 (59.4%) | 51 (51%) |
| Unresolved and complex | ≤ 1.06 | > 1.175 | 196 (11.3%) | 94 (10.6%) | 90 (11.9%) | 12 (12%) |
| Resolved and simple | > 1.06 | ≤ 1.175 | 483 (27.8%) | 272 (30.8%) | 181 (24%) | 30 (30%) |
| Resolved and complex | > 1.06 | > 1.175 | 97 (5.6%) | 55 (6.2%) | 35 (4.6%) | 7 (7%) |

Note : Unresolved and resolved morphology is based on the ratio of total to peak FIRST flux densities (θ_{FIRST}), while simple and complex radio morphologies are based on the ratio of NVSS to FIRST total flux densities ($\theta_{\text{NVSS-FIRST}}$).

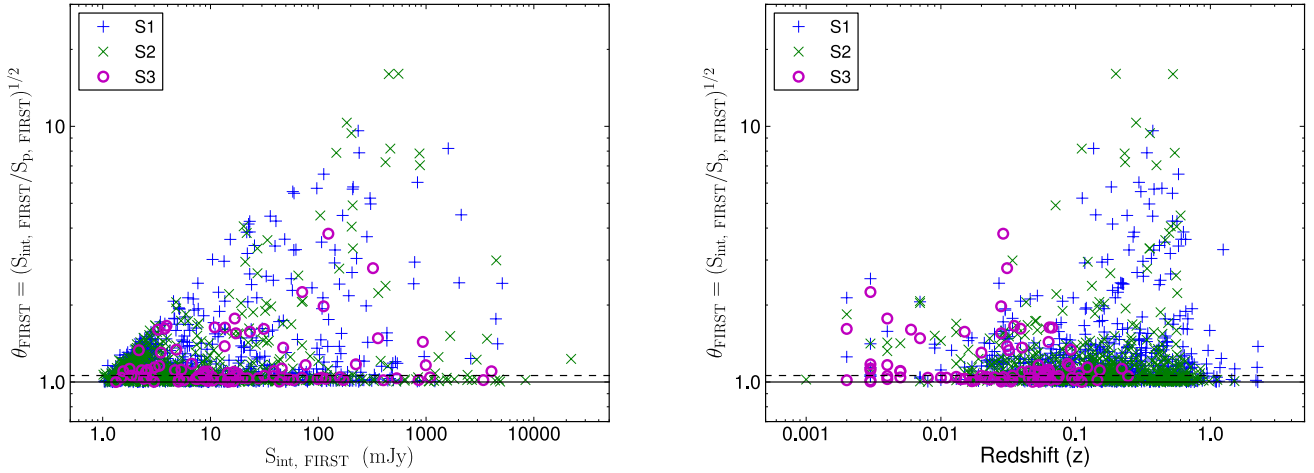


Figure 4. Left : θ_{FIRST} versus $S_{\text{int, FIRST}}$. Right : θ_{FIRST} versus Redshift. Seyfert 1s, Seyfert 2s and LINERs are shown by '+', 'x' and circles, respectively. Solid and dashed horizontal lines represents $\theta_{\text{FIRST}} = 1.0$ and $\theta_{\text{FIRST}} = 1.06$, respectively. Unresolved sources ($\theta_{\text{FIRST}} \leq 1.06$) are lying in between solid and dashed lines, while resolved sources ($\theta_{\text{FIRST}} > 1.06$) are lying above the dashed line.

~ 3.6 kpc ($\sim 60''$) along PA $\sim 135^\circ$ (see Figure 7, middle panel). The diffuse extended radio emission appear to align with the host galaxy major axis. This source possesses a complex radio structure with a slightly resolved core surrounded by a diffuse envelope of radio structure of $\sim 10''$ (0.9 kpc), roughly along the east-west direction (Nagar et al. 2002). The tapered maps have shown the ridge of emission spanning over ~ 3.6 kpc in north-south direction along the galaxy major axis.

(iii) NGC 7479, a Seyfert 1.9 galaxy at redshift (z) 0.0079, exhibits a curve-shaped extended emission along the north direction and a weaker southern component. The total extension of north to south component is ~ 9.2 kpc ($56''$). Beck et al. (2002) reported that NGC 7479 has strong polarized radio emission, mainly due to the nuclear jet.

The detailed study of the radio structures in all our sample LLAGN with multicomponent radio emission will be presented in our next paper. The FIRST images of three sources presented here show that KSRs in Seyferts and LINERs exhibit varying morphologies *e.g.*, linear, S-shaped, diffuse. This is consistent with previous studies based on more sensitive targeted radio observations of small

Seyfert samples (*e.g.*, Ulvestad & Wilson 1989; Kukula et al. 1993; Baum et al. 1993; Colbert et al. 1996; Gallimore et al. 2006).

7 NATURE OF KPC-SCALE RADIO EMISSION

We attempt to investigate the nature and origin of KSRs detected in Seyfert and LINER galaxies of our sample. We study radio luminosity distributions, radio-loudness parameters, the dependence KSRs radio power to the AGN power, ratios of radio-to-FIR fluxes and mid-IR colors to derive the statistical inferences about the origin of KSRs.

7.1 Radio luminosities

Figure 8 shows the radio luminosity distributions of unresolved and resolved sample sources detected in FIRST. It is evident that the luminosity distribution for unresolved sources can be represented by a normal distribution, while radio luminosity distribution of resolved sources is skewed towards higher radio luminos-

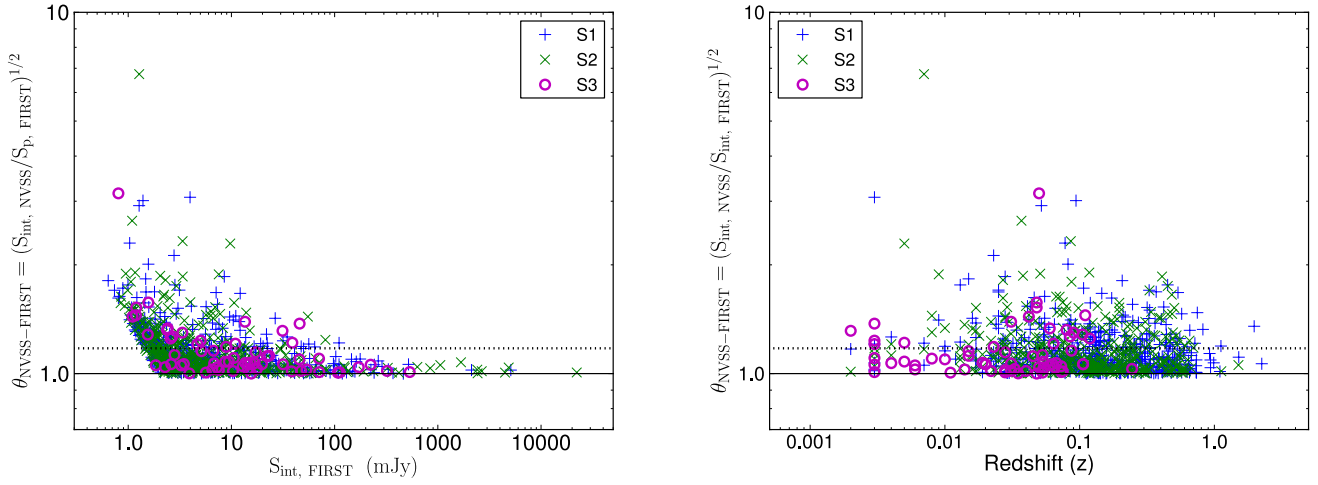


Figure 5. Left : $\theta_{\text{NVSS-FIRST}}$ versus $S_{\text{int, FIRST}}$. Right : $\theta_{\text{NVSS-FIRST}}$ versus redshift. Seyfert 1s, Seyfert 2s and LINERs are shown by '+', 'x' and circles, respectively. Solid and dotted horizontal lines represents $\theta_{\text{NVSS-FIRST}} = 1.0$ and $\theta_{\text{NVSS-FIRST}} = 1.175$, respectively. Simple sources ($\theta_{\text{NVSS-FIRST}} \leq 1.175$) are lying in between solid and dotted lines, while complex sources ($\theta_{\text{NVSS-FIRST}} > 1.175$) are lying above the dotted line.

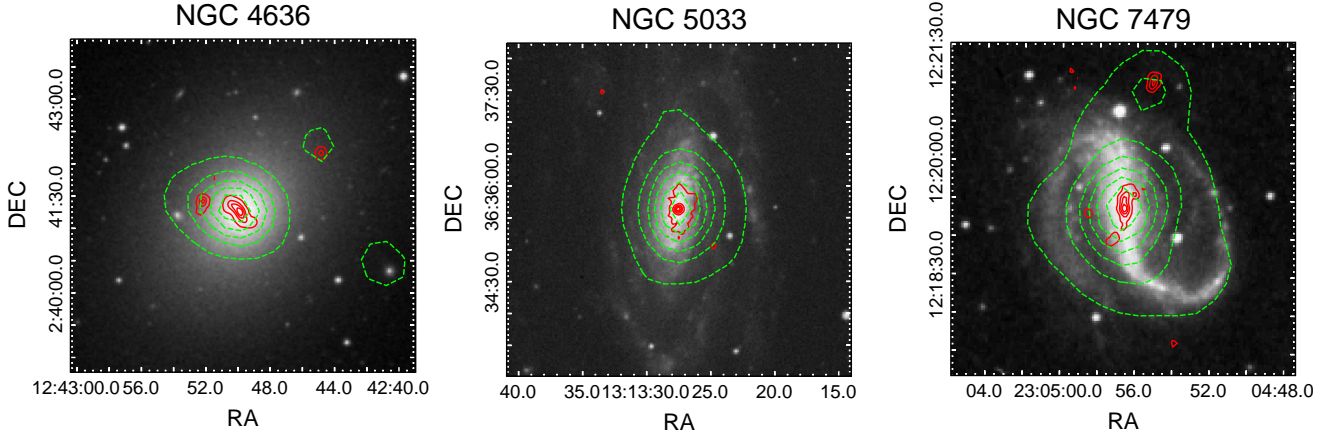


Figure 7. FIRST contours (in red solid curves) and NVSS contours (in green dotted curves) overplotted on the grey scale DSS optical images for NGC 4636 (left panel), NGC 5033 (middle panel) and NGC 7479 (right panel).

ity. Although, both unresolved sources ($\theta_{\text{FIRST}} \leq 1.06$) and resolved sources ($\theta_{\text{FIRST}} > 1.06$) have similar median radio luminosity values $\sim 2.25 \times 10^{23} \text{ W Hz}^{-1}$ and $\sim 1.98 \times 10^{23} \text{ W Hz}^{-1}$, respectively. The skewed distribution of resolved sources indicates that the resolved source population is relatively more dominant at higher radio luminosities.

To examine if the occurrence of KSRs is related to the total radio luminosity of a source we plot extended emission parameters θ_{FIRST} and $\theta_{\text{NVSS-FIRST}}$ versus 1.4 GHz FIRST total radio luminosity ($L_{\text{int, FIRST}}$). Figure 9 shows the plots of θ_{FIRST} versus $L_{\text{int, FIRST}}$ (left panel), and $\theta_{\text{NVSS-FIRST}}$ versus $L_{\text{int, FIRST}}$ (right panel). We note that resolved and complex sources (*i.e.*, sources with $\theta_{\text{FIRST}} > 1.06$ and $\theta_{\text{NVSS-FIRST}} > 1.175$) are present across all luminosities ranging from $\sim 10^{19} \text{ W Hz}^{-1}$ to $\sim 10^{29} \text{ W Hz}^{-1}$. This shows that KSRs are found in sources of low as well as high radio luminosities. We further note that a small fraction ($90/827 \sim 11\%$) of KSR sources characterized with high $\theta_{\text{FIRST}} (> 2)$ are preferentially found at high radio luminosities *i.e.*, $L_{1.4 \text{ GHz}} > 10^{24} \text{ W Hz}^{-1}$. The high ra-

dio luminosities ($L_{1.4 \text{ GHz}} \sim 10^{24} - 10^{28} \text{ W Hz}^{-1}$) of these sources imply that they are radio-loud AGN wherein $L_{1.4 \text{ GHz}} \sim 10^{24.5} \text{ W Hz}^{-1}$ can be considered as the dividing line between FR-I and FR-II radio galaxies (Fanaroff & Riley 1974; Rafter et al. 2011). Sources with $\theta_{\text{FIRST}} > 2$ means that extranuclear flux density is three times of the peak flux density which in turn makes them extended-emission-dominated radio sources. Indeed, several optically classified Seyfert galaxies are known to be radio-loud AGN with lobe-dominated KSRs (see Doi et al. (2012)). Moreover, we note that the sources of high radio luminosities ($L_{1.4 \text{ GHz}} > 10^{24} \text{ W Hz}^{-1}$) may have radio galaxy contaminants that are either incorrectly classified as Seyfert galaxies or there seems to be a population of sources that can be classified as radio galaxies based on its radio properties but optical properties are similar to Seyfert galaxies. In general, Seyfert galaxies are found to be hosted in late-type disk or lenticular galaxies (Schawinski et al. 2011), while radio-loud AGN are mainly hosted in early-type galaxies (Best et al. 2005). However, in recent times a few examples of radio galaxies hosted in disk

Table 3. Comparison of detected fraction KSR sources

| Reference | ν (GHz) | Telescope Configuration | Resolution (arcsec) | Sensitivity (5σ) (mJy) | N(Total) | N(KSRs) | Detection fraction |
|--------------------------|----------------|----------------------------|------------------------|------------------------------------|----------|---------|--------------------|
| Thean et al. (2000) | 8.4 | VLA A | ~ 0.25 | ~ 0.28 | 60 | 4 | $\sim 6.7\%$ |
| Kukula et al. (1995) | 8.4 | VLA A | ~ 0.25 | ~ 0.35 | 18 | 0 | 0.0 % |
| Ulvestad & Wilson (1989) | 1.4 | VLA A/B | ~ 2.0 | ~ 0.40 | 57 | 13 | $\sim 23\%$ |
| Gallimore et al. (2006) | 5.0 | VLA D | $\sim 15 - 20$ | ~ 0.25 | 43 | 19 | $\sim 44\%$ |
| <i>Our work</i> | | | | | | | |
| FIRST sample | 1.4 | VLA B | ~ 5 | ~ 1.0 | 2651 | 794 | $\sim 30.0\%$ |
| FIRST-NVSS sample | 1.4 | VLA D | ~ 45 | ~ 2.5 | 1737 | 738 | $\sim 42.3\%$ |

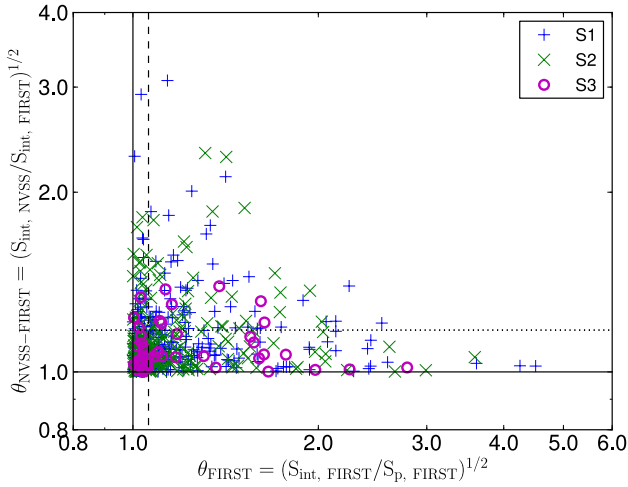


Figure 6. $\theta_{\text{NVSS-FIRST}}$ versus θ_{FIRST} . Seyfert 1s, Seyfert 2s and LINERs are shown by '+', 'x' and circles, respectively. Dashed vertical line represents dividing line ($\theta_{\text{FIRST}} = 1.06$) between resolved and unresolved sources detected in FIRST. Dotted horizontal line represents dividing line ($\theta_{\text{NVSS-FIRST}} = 1.175$) between simple and complex sources detected in NVSS. It is evident that there is no systematic trend and sources of variety of radio morphologies are present in our sample.

galaxies have also been reported (*e.g.*, NGC 612, Emonts et al. (2008); Specia, Hota et al. (2011); PKS 1814-637, Morganti et al. (2011), J2345-0449, Bagchi et al. (2014)). The optical and mid-IR properties of host galaxy ISM of these sources often show more in common with Seyfert galaxies than they do with radio galaxies (Morganti et al. 2011). Therefore, a detailed investigation on the properties of host galaxies and ISM of radio powerful Seyfert galaxies is required to confirm their nature.

Furthermore, unlike sources with high θ_{FIRST} , several sources with high NVSS-to-FIRST flux density ratios (say $\theta_{\text{NVSS-FIRST}} > 1.5$) are found at lower radio luminosities. A comparison of radio luminosity distributions of simple ($\theta_{\text{NVSS-FIRST}} \leq 1.175$) and complex radio sources ($\theta_{\text{NVSS-FIRST}} \geq 1.175$) shows that the complex sources indeed have systematically lower radio luminosities (with median radio luminosity $L_{1.4 \text{ GHz, FIRST, median}} \sim 5.1 \times 10^{22} \text{ W Hz}^{-1}$) than simple sources (with median radio luminosity $L_{1.4 \text{ GHz, FIRST, median}} \sim 4.4 \times 10^{23} \text{ W Hz}^{-1}$). This implies that low-surface-brightness extended radio emission detected by NVSS is more often present in low luminosity sources. Thus, the additional radio emission detected in NVSS may have significant contribution from star-formation as AGN are relatively weaker.

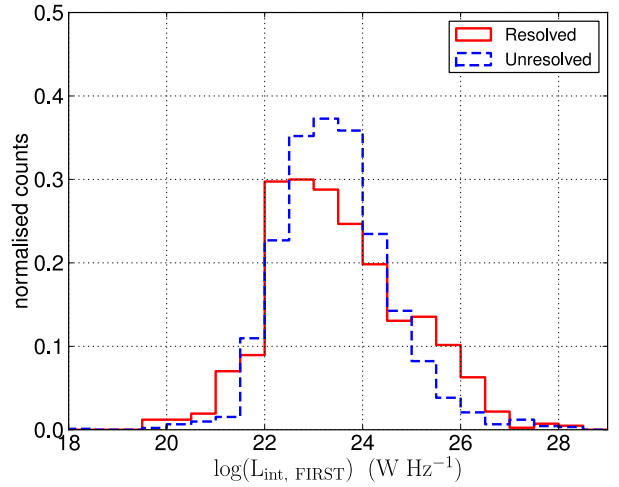


Figure 8. Distributions of FIRST 1.4 GHz radio luminosities ($L_{\text{int, FIRST}}$) for unresolved and resolved sources.

7.2 Radio loudness

In general, radio source population is known to exhibit bimodal distribution of radio-loudness parameter (R) with dividing line at $R = 10$ that categories radio sources into radio-quiet ($R < 10$) and radio-loud ($R \geq 10$), where R is defined as the ratio of monochromatic 5 GHz radio luminosity to the 4400 Å optical luminosity ($R = \frac{\nu_{5\text{GHz}} L_{5\text{GHz}}}{\nu_{4400\text{\AA}} L_{4400\text{\AA}}}$) (Visnovsky et al. 1992; Kellermann et al. 1994). The physical origin of the bimodality is generally attributed to the differences in the fundamental parameters of AGN-galaxy system such as the mass and spin of black hole, accretion rate and the Hubble type of host galaxy (Laor 2000; McLure & Jarvis 2004; Sikora et al. 2007; Rafter et al. 2011). Therefore, the degree of radio-loudness can be used to characterize the nature of AGN. We study radio-loudness of our sample sources to investigate if the presence of KSRs is related to radio-loudness. We derive 5 GHz radio luminosity ($L_{5 \text{ GHz}}$) for our sample sources from 1.4 GHz radio luminosity ($L_{1.4 \text{ GHz}}$) using a typical radio spectral index of -0.7 for Seyfert galaxies (Morganti et al. 1999; Singh et al. 2013). The optical continuum luminosity at 4400 Å ($L_{4400\text{\AA}}$) is derived from 5100 Å luminosity ($L_{5100\text{\AA}}$) using a typical optical spectral index of -0.5 (Sikora et al. 2007). The 5100 Å luminosity ($L_{5100\text{\AA}}$) is empirically estimated from H_{α} luminosity as both are found to be related to bolometric luminosity (McLure & Jarvis 2004; Greene & Ho 2005). Thus, 4400 Å luminosity ($L_{4400\text{\AA}}$) can be estimated from H_{α} luminosity as: $L_{4400\text{\AA}} = L_{5100\text{\AA}} \left(\frac{4400\text{\AA}}{5100\text{\AA}} \right)^{-0.5} = (2.59$

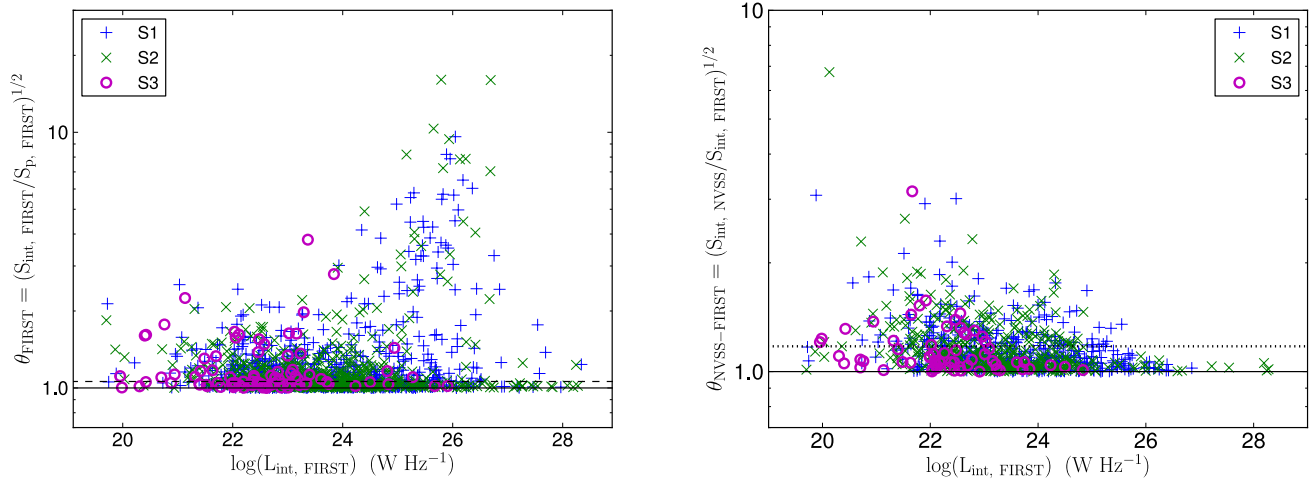


Figure 9. *Left:* θ_{FIRST} versus $L_{1.4 \text{ GHz, FIRST}}$. Dashed horizontal line represents ($\theta_{\text{FIRST}} = 1.06$) dividing line between unresolved and resolved sources. *Right:* $\theta_{\text{NVSS-FIRST}}$ versus $L_{1.4 \text{ GHz, FIRST}}$. Dotted horizontal line represents dividing line ($\theta_{\text{NVSS-FIRST}} = 1.175$) between simple and complex sources detected in NVSS. Seyfert 1s, Seyfert 2s and LINERs are shown by '+', 'x' and circles, respectively.

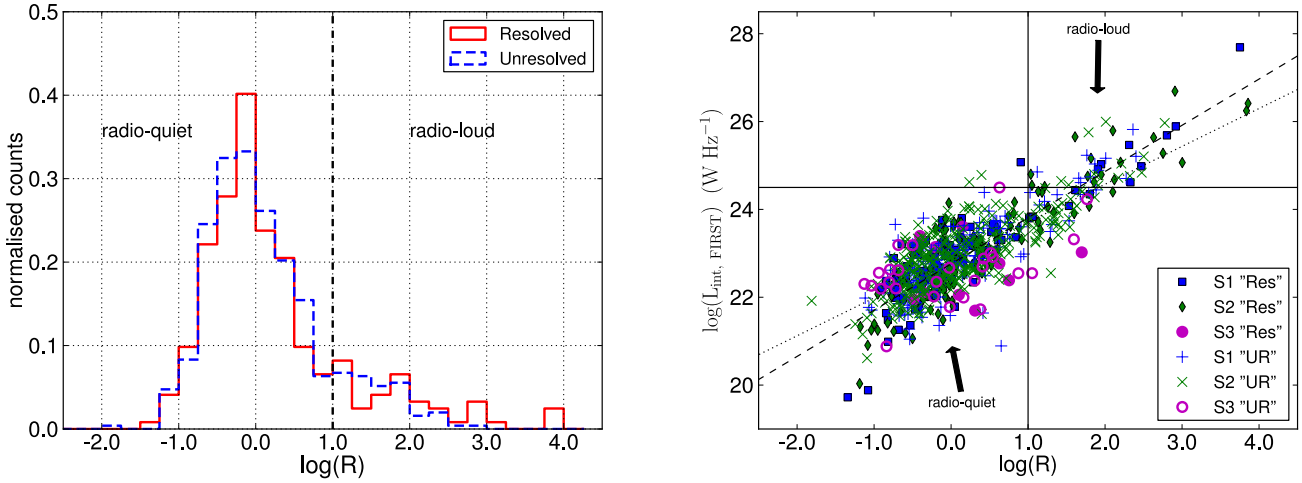


Figure 10. *Left :* Distributions of radio-loudness parameter for unresolved ($\theta_{\text{FIRST}} \leq 1.06$) and resolved ($\theta_{\text{FIRST}} > 1.06$) sources. Dotted vertical line is dividing line between radio-quiet and radio-loud population. *Right :* Radio luminosity versus radio loudness plot. Dashed and dotted lines represent least square regression lines for resolved ("Res") sources ($\log L_{\text{int, FIRST}} = 1.05 \log R + 22.76$) and unresolved ("UR") sources ($\log L_{\text{int, FIRST}} = 0.86 \log R + 22.76$), respectively. Solid Vertical line at $\log R = 1.0$ and solid horizontal line at $\log L_{\text{int, FIRST}} = 24.5$ W Hz⁻¹ represent conventional dividing line between radio-quiet and radio-loud sources. Filled and open symbols represent resolved and unresolved radio sources, respectively.

$\times 10^{43}$) ($\frac{L_{\text{H}\alpha}}{10^{42}}$)^{0.86} erg s⁻¹ (see Rafter et al. 2009). The $H_{\alpha, 6563\text{\AA}}$ flux for our sample sources is obtained from SDSS DR10. There are only $\sim 749/2651$ sources with $H_{\alpha, 6563\text{\AA}}$ flux available from SDSS DR10 and therefore our analysis on radio-loudness is limited only to this subsample. Figure 10 shows the distribution of radio loudness parameter for extended (KSRs) and compact (non-KSRs) radio sources of our sample. We find that both extended and compact radio sources show similar distributions of radio loudness parameter. As expected majority ($\sim 85\%$) of our Seyfert/LINER sample sources are radio-quiet ($R < 10$), while $\sim 15\%$ sources fall into the radio-loud ($R \geq 10$) category. We find that radio loudness parameter is correlated with total radio luminosity for both compact (unresolved) and extended (resolved) sources (see Figure 10, right panel). Spearman rank correlation coefficients for unresolved and

resolved sources are ~ 0.70 and 0.78 , respectively. The observed correlation is consistent with previous studies characterizing radio loudness in terms of radio-luminosity (e.g., Rafter et al. 2009). It is evident that most of the radio powerful sources ($L_{1.4 \text{ GHz}} \geq 10^{24.5}$ W Hz⁻¹) are radio-loud, while radio weak ($L_{1.4 \text{ GHz}} \leq 10^{23}$ W Hz⁻¹) are found to be radio-quiet. Moreover, a small fraction ($\sim 10\%$) of our sample sources with 1.4 GHz radio luminosity ($L_{1.4 \text{ GHz}} \sim 10^{23} - 10^{24.5}$ W Hz⁻¹) can be classified as radio-intermediate with radio loudness parameter ($R \sim 10 - 100$). The presence of powerful radio-loud sources ($R > 100$ and $L_{1.4 \text{ GHz}} \geq 10^{24.5}$ W Hz⁻¹), although only a very small fraction ($\sim 3.0\%$), is apparently unexpected as these sources can simply be categorized as FR-II radio galaxies. As discussed in the previous section, these sources are either radio galaxy contaminants or there is a population of sources in

which radio and optical properties give different classification. The radio-loudness versus radio luminosity plot for our sample sources suggests that radio-loudness parameter in Seyfert, LINER galaxies is distributed in a continuous fashion and overlaps with that of FR-I/FR-II radio galaxies. This is consistent with Kharb et al. (2014) results showing the overlap in the radio-loudness of Seyfert galaxies and FR-I radio galaxies with $\sim 11\%$ of Seyfert galaxies in their sample classified as radio-loud. Using a sample of broad line AGN Rafter et al. (2009) also found no clear demarcation between the radio-loud ($R \geq 10$) and radio-quiet ($R < 10$) sources but instead fill in a more radio-intermediate population in a continuous fashion. Finally, we note that the presence of KSRs in Seyfert and LINER galaxies does not seem to have any dependence on the radio-loudness as both extended (KSRs) and compact (non-KSRs) sources show similar distribution of radio-loudness parameter.

7.3 KSR radio power versus AGN power

A test on the correlation between the strength of kpc-scale radio emission and the AGN power may provide clues about the origin of KSRs. A positive correlation between the radio power of KSRs and AGN power can be expected if KSRs are powered by AGN. We use core radio power, $O[III] \lambda 5007 \text{ \AA}$ luminosity as the proxies for AGN power. We derive extended emission from total emission subtracted by peak emission ($S_{\text{ext}} = S_{\text{int, FIRST}} - S_{\text{peak, FIRST}}$) and FIRST peak flux density is considered as core radio emission. However, we caution that our estimates of core and extended radio emission (L_{core}) using FIRST peak emission are fairly crude as the FIRST peak flux density may contain extended emission in high- z sources and in type 1 sources where AGN jets are oriented towards observer. High resolution observations detecting core radio emission at parsec-scale would give more robust estimates of core radio emission, but high resolution radio data are not available for our sample sources. To get more accurate estimate of core and extended radio emission we create a subsample of low redshift sources ($z \leq 0.01$) for which FIRST beam of $5''$ corresponds to ≤ 1.0 kpc and thus give better segregation of core and extended emission. However, number of such sources is too small with limited span in luminosity space to give a robust statistical result.

7.3.1 KSR radio power versus core radio power

The nuclear radio emission is optically thin to torus dust obscuration and also jets in Seyfert and LINER galaxies are not relativistically beamed (Middelberg et al. 2004; Ulvestad et al. 2005). Therefore, AGN core radio emission can be considered an isotropic property in Seyfert galaxies that provides an orientation-independent measurement of AGN power (Kukula et al. 1995; Xu et al. 1999; Thean et al. 2001). To check if extended KSRs emission is related to the AGN core radio power we plot radio luminosity of extended emission versus core radio luminosity, Figure 11 (left panel) shows that the core radio luminosity is positively correlated with the radio luminosity of extended emission component. Spearman rank correlation test gives correlation coefficient (ρ) = 0.94 with the probability of two parameters being uncorrelated ($p < 2.2 \times 10^{-16}$). We also performed statistical test on the correlation between core radio flux density ($S_{\text{core}} = S_{\text{peak, FIRST}}$) and extended radio flux density ($S_{\text{ext}} = S_{\text{int, FIRST}} - S_{\text{peak, FIRST}}$). Spearman rank correlation test results correlation coefficient (ρ) = 0.69 with the probability of two parameters being uncorrelated ($p < 1.0 \times 10^{-16}$). This demonstrates that correlation between core radio luminosity and extended radio

emission luminosity is not driven by distance effect. The correlation between core radio luminosity and extended radio emission luminosity can be interpreted as more powerful AGN tend to show more powerful KSRs and therefore, inferring that KSRs are likely to be powered by AGN. Sources with $L_{\text{core}} > L_{\text{ext}}$ can be considered as core-dominated sources while sources with $L_{\text{core}} < L_{\text{ext}}$ are extended-emission-dominated sources. From figure 11 it is evident that extended-emission-dominated sources are preferentially found at higher radio luminosities ($L_{\text{core}} > 10^{23} \text{ W Hz}^{-1}$), which is also inferred from the θ_{FIRST} versus $L_{1.4\text{GHz, FIRST}}$ plot (see Figure 9).

7.3.2 KSR radio power versus $[O III] \lambda 5007 \text{ \AA}$ line luminosity

$[O III] \lambda 5007 \text{ \AA}$ line emission is believed to originate from narrow line region and is found to be correlated with nuclear ionizing continuum, as well as nuclear X-ray luminosity, and therefore is considered as the proxy for intrinsic AGN power (Nelson & Whittle 1995; Heckman et al. 2005). Also, it is unaffected by the torus obscuration as it originates outside the torus. Figure 11 (right panel) shows an increasing trend of KSRs extended emission radio luminosity (L_{ext}) with $[O III]$ luminosity, however with a large scatter. Spearman rank correlation test yields correlation coefficient (ρ) = 0.59 with the probability of two parameters being uncorrelated ($p < 1.0 \times 10^{-16}$). The apparent correlations between extended emission (KSRs) radio luminosity (L_{ext}) and $[O III] \lambda 5007 \text{ \AA}$ line emission luminosity ($L_{[O III] 5007 \text{ \AA}}$) can be interpreted if extended radio emission is related to AGN power. If $[O III] \lambda 5007 \text{ \AA}$ line luminosity is considered as the accurate measure of AGN power then the large scatter can be understood if KSRs emission is influence by other factors such as the contamination from star formation, presence of circumnuclear starburst and the variation in the type of host galaxy.

7.4 Ratio of FIR-to-radio flux

Star-forming galaxies are known to display a tight correlation between far-infrared and radio continuum emission as both FIR and radio emission are believed to be linked to star-formation activity (Condon 1992; Kovács et al. 2006; Sargent et al. 2010). However, AGN exhibit radio excess due to additional radio emission from AGN core and jets, and tend to deviate from typical radio-FIR correlation (Yun et al. 2001; Morić et al. 2010). AGN galaxies can be expected to show tighter radio-FIR correlation if radio emission component from AGN is subtracted out. Using a sample of Seyfert galaxies Baum et al. (1993) reported that extranuclear radio power derived by subtracting nuclear radio power from the total radio power exhibit tighter correlation with the total FIR luminosity. Following a similar approach we use radio-FIR correlation to examine whether KSRs are powered by AGN or star-formation. In Seyfert and LINER galaxies, if extranuclear KSR emission is attributed to star-formation and nuclear emission is solely from AGN core then extranuclear radio emission is expected to show tighter correlation with total FIR emission. We derive extranuclear KSRs radio emission (S_{ext}) by subtracting FIRST peak emission (S_{peak}) from the NVSS total radio emission (S_{total}) and assume that the FIRST peak radio emission is primarily from AGN core.

We investigate the ratio of FIR to radio continuum (q parameter) for our KSR sample sources using both total and extranuclear radio emission. The ratio of FIR to radio continuum is defined as $q = \log[(\text{FIR}/3.75 \times 10^{12} \text{ Hz})/S_{1.4 \text{ GHz}}]$, where $\text{FIR} = 1.26 \times 10^{-14} [2.58 S_{60 \mu\text{m}} + S_{100 \mu\text{m}}] \text{ W m}^{-2}$ (Helou et al. 1985). The FIR

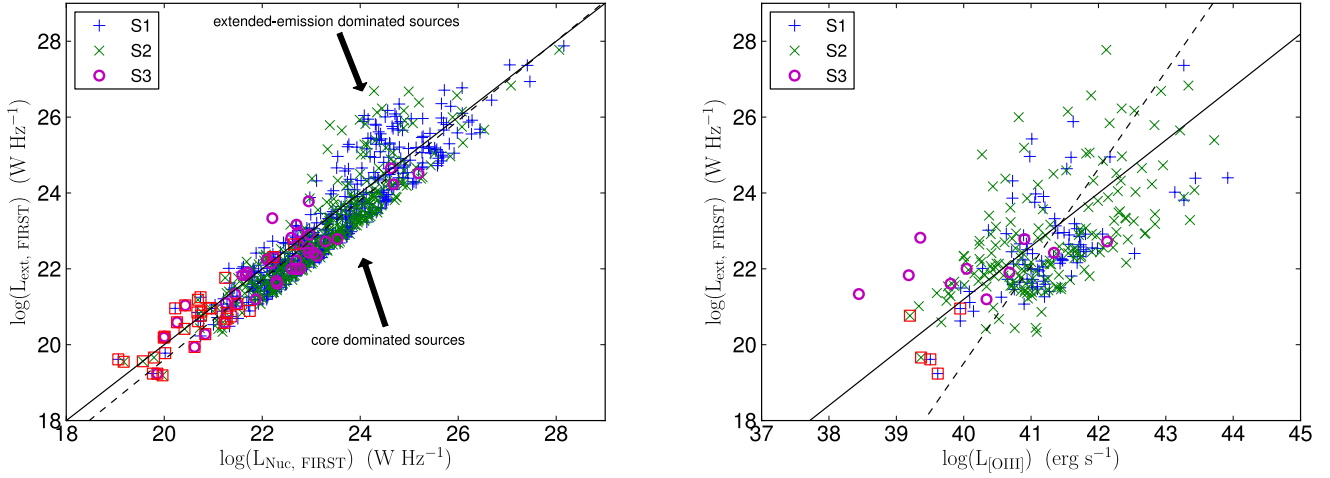


Figure 11. *Left* : $L_{\text{ext, FIRST}}$ versus $L_{\text{Nuc, FIRST}}$. Solid line represents bisector ($L_{\text{core, FIRST}} = L_{\text{ext, FIRST}}$) while dashed line represents least square regression line ($L_{\text{ext, FIRST}} = 1.05 L_{\text{core, FIRST}} - 1.39$). *Right* : $L_{\text{ext, FIRST}}$ versus $L_{\text{OIII } \lambda 5007\text{\AA}}$ plot. Solid line represents bisector ($L_{\text{OIII}} = 0.69 L_{\text{ext, FIRST}} + 25.64$) while dashed line represents least square regression line ($L_{\text{OIII}} = 0.39 L_{\text{core, FIRST}} + 32.39$). Seyfert 1s, Seyfert 2s and LINERs are shown by '+', 'x' and circles, respectively. Square symbols represent sources with redshift ($z \leq 0.01$) for which FIRST beam of $\sim 5''.0$ corresponds to ≤ 1.0 kpc and thereby gives a more robust separation of nuclear (core) and extranuclear (extended) emission.

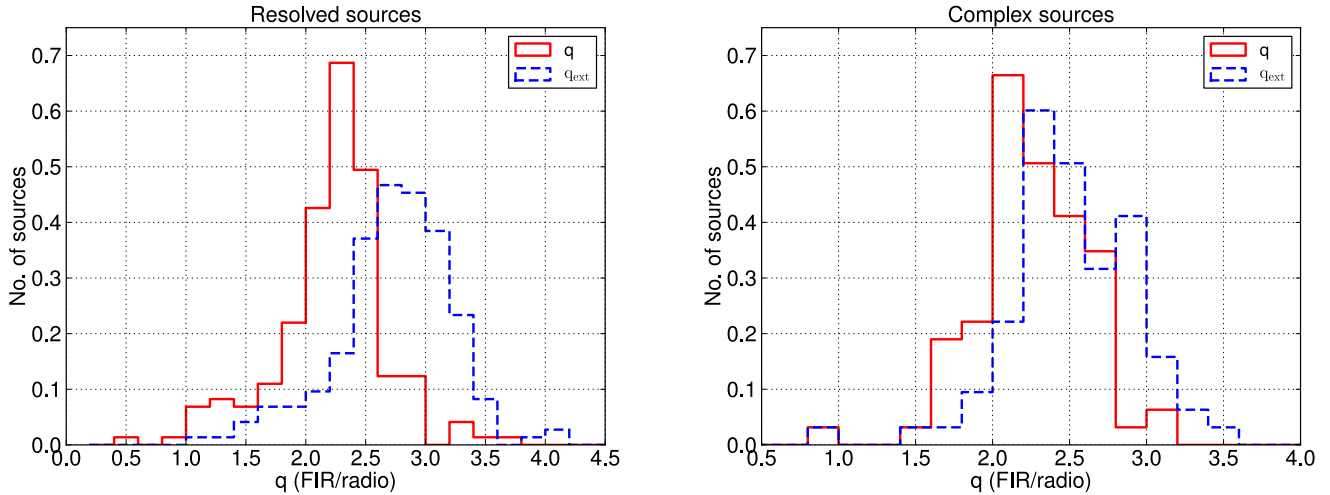


Figure 12. *Left* : Distribution of the ratio of FIR to 1.4 GHz radio continuum (q) for resolved radio sources ($\theta_{\text{FIRST}} > 1.06$). *Right* : Distribution of the ratio of FIR to 1.4 GHz radio continuum (q) for complex radio sources ($\theta_{\text{FIRST-NVSS}} > 1.175$). For resolved and complex sources the parameter q is estimated using total 1.4 GHz radio emission detected in FIRST and NVSS, respectively. Parameter q_{ext} for resolved and complex sources is estimated using only extranuclear radio emission ($S_{\text{ext, FIRST}} = S_{\text{int, FIRST}} - S_{\text{peak, FIRST}}$ and $S_{\text{ext, NVSS}} = S_{\text{int, NVSS}} - S_{\text{peak, FIRST}}$) detected in FIRST and NVSS, respectively.

fluxes at $60 \mu\text{m}$ and $100 \mu\text{m}$ are obtained from InfraRed Astronomical Survey (IRAS³) and are in Jy units. Using IRAS observations we find FIR counterparts of only 217/776 $\sim 28\%$ KSR sources and therefore our investigation on radio-FIR correlation is limited to FIR detected subsample. Fig 12 shows the distributions of the ratio of FIR to radio (q parameter) for resolved ($\theta_{\text{FIRST}} > 1.06$) and complex ($\theta_{\text{FIRST-NVSS}} > 1.175$) KSR sources. We find that both resolved and complex sources exhibit wide range of q values over 0.5 to 4.0 with median values ~ 2.27 and 2.21 , respectively, with standard deviations 0.56 and ~ 0.37 , respectively. The average value

of q parameter for star-forming galaxies in the local universe is found to be $(q) \sim 2.3$, and it decreases for AGN-bearing galaxies (Sargent et al. 2010). The lower median value and wide distribution of q parameter for our (resolved and complex) KSR sources is indicative of the presence of AGN.

We also estimate the ratio of FIR-to-radio (q_{ext}) using extranuclear flux density for resolved and complex KSR sources. The extranuclear radio emission for KSR sources is derived by subtracting FIRST peak flux density from total FIRST and NVSS flux density, respectively (*i.e.*, $S_{\text{ext, FIRST}} = S_{\text{int, FIRST}} - S_{\text{peak, FIRST}}$ and *i.e.*, $S_{\text{ext, NVSS}} = S_{\text{int, NVSS}} - S_{\text{peak, FIRST}}$). We note that that both resolved and complex KSR sources show an even wider distribution of q_{ext} spanning over 0.5 to 4.5 with median values ~ 2.77 and

³ <http://irsa.ipac.caltech.edu/Missions/iras.html>

2.46 respectively and standard deviation ~ 0.58 and 0.41 , respectively. The wider distribution of q_{ext} compared to q suggests that extranuclear KSR radio emission is likely to be powered by AGN (e.g., Roy et al. 1998). The higher median values of q_{ext} can be understood if extranuclear total radio emission is underestimated as the FIRST peak emission can have significant contribution from star-formation. The dusty torus around AGN may also contribute significantly to total FIR emission and can result in a higher value of q_{ext} parameter.

7.5 Mid-IR colors

IR colors can be used to measure the relative contribution of a starburst or AGN to the total bolometric luminosity, with redder (cooler) colors characterizing the dominance of starburst (Rush et al. 1993; Dopita et al. 1998; Lacy et al. 2004; Stern et al. 2012). We use mid-IR color-color diagram to check if KSR sources are dominated by starburst or AGN using *Wide-field Infrared Survey Explorer (WISE)*⁴ data. WISE covers all sky in four mid-IR bands i.e., W1 [3.4 μm], W2 [4.6 μm], W3 [12 μm], and W4 [22 μm] with an angular resolution of 6.1, 6.4, 6.5, and 12 arcsec, respectively. WISE counterparts of our sources are found using a search radius of $2''.0$ around the optical positions. Only 752/827 sources (91%) with extended radio emission have WISE counterparts.

In the literature, several mid-IR color-color diagnostics have been developed for separating AGN and star-forming normal galaxies (e.g., Lacy et al. 2004; Stern et al. 2005) and WISE colors have been used to identify AGN (e.g., Stern et al. 2012; Mateos et al. 2012)). We use WISE color-color diagrams of our sample sources, where the AGN selection wedge is defined as: $W1 - W2 \geq 0.315 \times (W2 - W3) - 0.222$ and $W1 - W2 \geq 0.315 \times (W2 - W3) + 0.796$ and $W1 - W2 = -3.172 \times (W2 - W3) + 7.624$ (see Mateos et al. 2012). Using 22 μm WISE band is not much useful due to its significantly shallower depth in comparison to the first three bands and also star formation contribution is likely to increase at 22 μm (Mateos et al. 2012). Figure 13 shows that KSR sources have a wide range of IR colors with majority of them falling into AGN wedge. We note that, in general, sources within the AGN selection wedge are radio powerful sources while sources falling outside the AGN wedge are of relatively lower radio luminosities. This can be understood if mid-IR emission is dominated by AGN in radio powerful sources ($L_{1.4\text{GHz}} \geq 10^{24} \text{ W Hz}^{-1}$), while in sources with relatively lower radio luminosity mid-IR emission apparently have greater contribution from dust heated by stars. Therefore, KSRs in radio luminous sources are likely to be powered by AGN. On the other hand, in sources of relatively low radio luminosities, KSRs can have contribution from starformation. Moreover, we caution that the WISE mid-IR colors cuts should be used with care as these color cuts may be biased against heavily obscured type-2 AGN. Also, there are suggestions that radio selected AGN may have a different accretion mode, i.e., radiatively inefficient (radio mode), and may not strictly follow the mid-IR color selection criteria (Hardcastle et al. 2007; Griffith & Stern 2010).

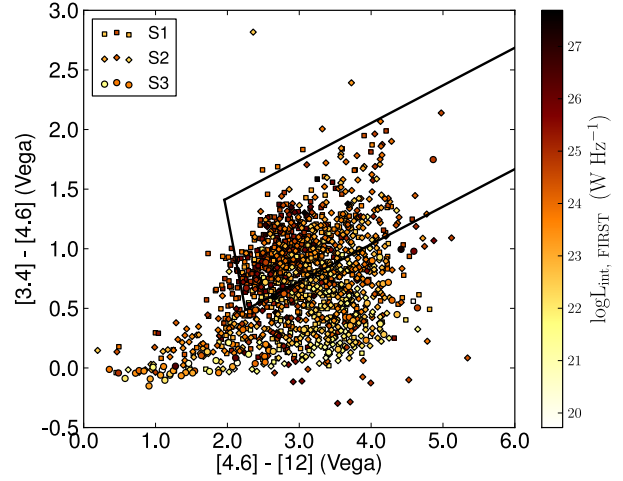


Figure 13. WISE mid-IR colors for KSR sources. Solid lines show the AGN wedge defined as: $W1 - W2 > 0.315 \times (W2 - W3) - 0.222$ and $W1 - W2 < 0.315 \times (W2 - W3) + 0.796$ and $W1 - W2 = -3.172 \times (W2 - W3) + 7.624$ (Mateos et al. 2012).

8 CONCLUSIONS

We have studied the prevalence and nature of KSRs in Seyfert and LINER galaxies using 1.4 GHz VLA FIRST and NVSS observations. Our sample is the largest sample hitherto used for KSR studies and consists of 2651 sources detected in FIRST. Of these, 1737 sources also have NVSS counterparts. Similar redshift distributions of Seyfert type 1s and type 2s suggests that our sample is not affected by biases introduced by dust obscuration. Conclusions of our study are outlined as below.

(i) Using a concentration parameter based on the ratio of total-to-peak flux density $\theta_{\text{FIRST}} = (S_{\text{int, FIRST}}/S_{\text{peak, FIRST}})^{1/2}$, we find $\geq 30\%$ KSR sources (i.e., sources with radio structures larger than 1.0 kpc) in the FIRST detected sample. The comparison of NVSS to FIRST flux densities help us in detecting faint extended radio emission that is resolved out in FIRST observations and we obtain $\geq 42\%$ KSR sources in FIRST-NVSS subsample. This fraction of KSR sources is only a lower limit owing to the combined effects of projection, resolution and sensitivity. The comparison of the fraction of KSRs detected in our sample with the previous studies demonstrates the importance of low-frequency observations with relatively lower resolution in detecting KSRs efficiently.

(ii) There are a total of 180 Seyfert and LINER galaxies in our sample that exhibit multicomponent KSRs in FIRST observations. We find that these sources display varying morphologies e.g., linear, S-shaped and diffuse, which is consistent with the previous studies based on sensitive targeted observations of small samples.

(iii) We find that KSR sources are distributed across all redshifts, luminosities and radio-loudness. We show that the presence of KSRs in Seyfert and LINER galaxies does not seem to have any dependence on the radio luminosity and radio-loudness. A small fraction ($\sim 10\% - 15\%$) of KSR sources characterized with high total-to-peak flux density ratio and high radio luminosity ($L_{1.4\text{GHz}} > 10^{24} \text{ W Hz}^{-1}$) are radio-loud. These sources may constitute a population of radio powerful Seyfert and LINER galaxies with radio properties overlapping with radio galaxies.

(iv) We find that the extranuclear radio power in KSR sources is

⁴ <http://irsa.ipac.caltech.edu/Missions/wise.html>

positively correlated with the core radio power and [O III] λ 5007Å line luminosity. This can be interpreted as KSRs are powered by AGN rather than star-formation.

(v) The ratio of FIR-to-radio continuum (q parameter) for KSR sources shows a wide distribution spanning over 0.5 to 4.0 with median value lower than that for typical starforming galaxies and thus indicating the dominance of AGN radio emission. The ratio of FIR-to-radio continuum (q_{ext}) using extranuclear radio flux density (derived by subtracting FIRST peak flux density from NVSS total flux density) shows an even wider distribution suggesting that the extranuclear KSR radio emission is likely to be originated from AGN.

(vi) The mid-IR color-color diagram for KSR sources shows that the mid-IR emission in radio powerful sources tends to be dominated by AGN, while in sources with lower radio luminosities mid-IR emission apparently have greater contribution from dust heated by stars. This can be understood if KSRs in radio luminous sources are primarily powered by AGN, while in sources with relatively low radio luminosities KSRs may have substantial contribution from star-formation.

ACKNOWLEDGMENTS

We acknowledge support from the Indo-French Center for the Promotion of Advanced Research (Centre Franco-Indien pour la Promotion de la Recherche Avance) under program no. 4404-3. This research has made use of the NASA/IPAC Extragalactic Database (NED) which is operated by the Jet Propulsion Laboratory, California Institute of Technology, under contract with the National Aeronautics and Space Administration. This publication makes use of data products from the Wide-field Infrared Survey Explorer, which is a joint project of the University of California, Los Angeles, and the Jet Propulsion Laboratory/California Institute of Technology, funded by the National Aeronautics and Space Administration. Funding for SDSS-III has been provided by the Alfred P. Sloan Foundation, the Participating Institutions, the National Science Foundation, and the U.S. Department of Energy Office of Science. The SDSS-III web site is <http://www.sdss3.org/>. SDSS-III is managed by the Astrophysical Research Consortium for the Participating Institutions of the SDSS-III Collaboration including the University of Arizona, the Brazilian Participation Group, Brookhaven National Laboratory, Carnegie Mellon University, University of Florida, the French Participation Group, the German Participation Group, Harvard University, the Instituto de Astrofísica de Canarias, the Michigan State/Notre Dame/JINA Participation Group, Johns Hopkins University, Lawrence Berkeley National Laboratory, Max Planck Institute for Astrophysics, Max Planck Institute for Extraterrestrial Physics, New Mexico State University, New York University, Ohio State University, Pennsylvania State University, University of Portsmouth, Princeton University, the Spanish Participation Group, University of Tokyo, University of Utah, Vanderbilt University, University of Virginia, University of Washington, and Yale University.

REFERENCES

- Bagchi J., Vivek M., Vikram V., Hota A., Biju K. G., Sirothia S. K., Srianand R., Gopal-Krishna Jacob J., 2014, *ApJ*, 788, 174
- Baum S. A., O’Dea C. P., Dallacassa D., de Bruyn A. G., Pedlar A., 1993, *ApJ*, 419, 553
- Beck R., Shoutenkov V., Ehle M., Harnett J. I., Haynes R. F., Shukurov A., Sokoloff D. D., Thierbach M., 2002, *A&A*, 391, 83
- Becker R. H., White R. L., Helfand D. J., 1995, *ApJ*, 450, 559
- Birkinshaw M., Davies R. L., 1985, *ApJ*, 291, 32
- Carilli C. L., Holdaway M. A., Ho P. T. P., de Pree C. G., 1992, *ApJL*, 399, L59
- Colbert E. J. M., Baum S. A., Gallimore J. F., O’Dea C. P., Christensen J. A., 1996, *ApJ*, 467, 551
- Condon J. J., 1992, *ARAA*, 30, 575
- Condon J. J., Cotton W. D., Greisen E. W., Yin Q. F., Perley R. A., Taylor G. B., Broderick J. J., 1998, *AJ*, 115, 1693
- de Vries W. H., Becker R. H., White R. L., 2006, *AJ*, 131, 666
- Doi A., Nagira H., Kawakatu N., Kino M., Nagai H., Asada K., 2012, *ApJ*, 760, 41
- Dopita M. A., Heisler C., Lumsden S., Bailey J., 1998, *ApJ*, 498, 570
- Emonts B. H. C., Morganti R., Oosterloo T. A., Holt J., Tadhunter C. N., van der Hulst J. M., Ojha R., Sadler E. M., 2008, *MNRAS*, 387, 197
- Fanaroff B. L., Riley J. M., 1974, *MNRAS*, 167, 31P
- Gallimore J. F., Axon D. J., O’Dea C. P., Baum S. A., Pedlar A., 2006, *AJ*, 132, 546
- Greene J. E., Ho L. C., 2005, *ApJ*, 630, 122
- Griffith R. L., Stern D., 2010, *AJ*, 140, 533
- Hardcastle M. J., Evans D. A., Croston J. H., 2007, *MNRAS*, 376, 1849
- Heckman T. M., Ptak A., Hornschemeier A., Kauffmann G., 2005, *ApJ*, 634, 161
- Helou G., Soifer B. T., Rowan-Robinson M., 1985, *ApJL*, 298, L7
- Ho L. C., Ulvestad J. S., 2001, *ApJS*, 133, 77
- Hota A., Sirothia S. K., Ohya Y., Konar C., Kim S., Rey S.-C., Saikia D. J., Croston J. H., Matsushita S., 2011, *MNRAS*, 417, L36
- Ivezic Z., Menou K., Knapp G. R., Strauss M. A., Lupton R. H., Vanden Berk D. E., Richards G. T., Tremonti C., Weinstein M. A., 2002, *AJ*, 124, 2364
- Kellermann K. I., Sramek R., Schmidt M., Shaffer D. B., Green R., 1989, *AJ*, 98, 1195
- Kellermann K. I., Sramek R. A., Schmidt M., Green R. F., Shaffer D. B., 1994, *AJ*, 108, 1163
- Kharb P., Hota A., Croston J. H., Hardcastle M. J., O’Dea C. P., Kraft R. P., Axon D. J., Robinson A., 2010, *ApJ*, 723, 580
- Kharb P., O’Dea C. P., Baum S. A., Colbert E. J. M., Xu C., 2006, *ApJ*, 652, 177
- Kharb P., O’Dea C. P., Baum S. A., Hardcastle M. J., Dicken D., Croston J. H., Mingo B., Noel-Storr J., 2014, *MNRAS*, 440, 2976
- Kharb P., Singh V., Gallimore J. F., Ishwara-Chandra C. H., 2014, *ArXiv:1402.1577 e-prints*
- Kimball A. E., Ivezić Ž., 2008, *AJ*, 136, 684
- Kovács A., Chapman S. C., Dowell C. D., Blain A. W., Ivison R. J., Smail I., Phillips T. G., 2006, *ApJ*, 650, 592
- Kukula M. J., Ghosh T., Pedlar A., Schilizzi R. T., 1999, *ApJ*, 518, 117
- Kukula M. J., Ghosh T., Pedlar A., Schilizzi R. T., Miley G. K., de Bruyn A. G., Saikia D. J., 1993, *MNRAS*, 264, 893
- Kukula M. J., Holloway A. J., Pedlar A., Meaburn J., Lopez J. A., Axon D. J., Schilizzi R. T., Baum S. A., 1996, *MNRAS*, 280, 1283

- Kukula M. J., Pedlar A., Baum S. A., O’Dea C. P., 1995, *MNRAS*, 276, 1262
- Lacy M., Storrie-Lombardi L. J., Sajina A., Appleton P. N., Armus L., Chapman S. C., Choi P. I., Fadda D., Yan L., 2004, *ApJS*, 154, 166
- Lal D. V., Shastri P., Gabuzda D. C., 2004, *A&A*, 425, 99
- Laor A., 2000, *ApJL*, 543, L111
- Lu Y., Wang T., Zhou H., Wu J., 2007, *AJ*, 133, 1615
- Mateos S., Alonso-Herrero A., Carrera F. J., Blain A., Watson M. G., Barcons X., Braito V., Severgnini P., Donley J. L., Stern D., 2012, *MNRAS*, 426, 3271
- McLure R. J., Jarvis M. J., 2004, *MNRAS*, 353, L45
- Middelberg E., Roy A. L., Nagar N. M., Krichbaum T. P., Norris R. P., Wilson A. S., Falcke H., Colbert E. J. M., Witzel A., Fricke K. J., 2004, *A&A*, 417, 925
- Momjian E., Romney J. D., Carilli C. L., Troland T. H., 2003, *ApJ*, 597, 809
- Morganti R., Holt J., Tadhunter C., Ramos Almeida C., Dicken D., Inskip K., Oosterloo T., Tzioumis T., 2011, *A&A*, 535, A97
- Morganti R., Tsvetanov Z. I., Gallimore J., Allen M. G., 1999, *Astron. & Astrophys. Suppl.*, 137, 457
- Morić I., Smolčić V., Kimball A., Riechers D. A., Ivezić Ž., Scoville N., 2010, *ApJ*, 724, 779
- Nagar N. M., Falcke H., Wilson A. S., 2005, *A&A*, 435, 521
- Nagar N. M., Falcke H., Wilson A. S., Ulvestad J. S., 2002, *A&A*, 392, 53
- Nelson C. H., Whittle M., 1995, *ApJS*, 99, 67
- Orienti M., Prieto M. A., 2010, *MNRAS*, 401, 2599
- Osterbrock D. E., 1981, *ApJ*, 249, 462
- Panessa F., Giroletti M., 2013, *MNRAS*, 432, 1138
- Rafter S. E., Crenshaw D. M., Wiita P. J., 2009, *AJ*, 137, 42
- Rafter S. E., Crenshaw D. M., Wiita P. J., 2011, *AJ*, 141, 85
- Roy A. L., Norris R. P., Kesteven M. J., Troup E. R., Reynolds J. E., 1998, *MNRAS*, 301, 1019
- Rush B., Malkan M. A., Spinoglio L., 1993, *ApJS*, 89, 1
- Sadler E. M., Slee O. B., Reynolds J. E., Roy A. L., 1995, *MNRAS*, 276, 1373
- Sargent M. T., Schinnerer E., Murphy E., Aussel H., Le Floc’h E., Frayer D. T., Martínez-Sansigre A., Oesch P., Salvato M., 2010, *ApJS*, 186, 341
- Schawinski K., Treister E., Urry C. M., Cardamone C. N., Simmons B., Yi S. K., 2011, *ApJL*, 727, L31
- Schmidt M., Green R. F., 1983, *ApJ*, 269, 352
- Seaquist E. R., Odegard N., 1991, *ApJ*, 369, 320
- Sikora M., Stawarz Ł., Lasota J.-P., 2007, *ApJ*, 658, 815
- Singh V., Shastri P., Ishwara-Chandra C. H., Athreya R., 2013, *A&A*, 554, A85
- Stanger V. J., Warwick R. S., 1986, *MNRAS*, 220, 363
- Stern D., Assef R. J., Benford D. J., Blain A., Cutri R., Dey A., Eisenhardt P., Griffith R. L., Jarrett T. H., Lake S., Masci F., Petty S., Stanford S. A., Tsai C.-W., Wright E. L., Yan L., Harrison F., Madsen K., 2012, *ApJ*, 753, 30
- Stern D., Eisenhardt P., Gorjian V., Kochanek C. S., Caldwell N., Eisenstein D., Brodwin M., Brown M. J. I., Cool R., Dey A., Green P., Jannuzi B. T., Murray S. S., Pahre M. A., Willner S. P., 2005, *ApJ*, 631, 163
- Thean A., Pedlar A., Kukula M. J., Baum S. A., O’Dea C. P., 2000, *MNRAS*, 314, 573
- Thean A., Pedlar A., Kukula M. J., Baum S. A., O’Dea C. P., 2001, *MNRAS*, 325, 737
- Ulvestad J. S., Neff S. G., Wilson A. S., 1987, *AJ*, 93, 22
- Ulvestad J. S., Wilson A. S., 1989, *ApJ*, 343, 659
- Ulvestad J. S., Wong D. S., Taylor G. B., Gallimore J. F., Mundell C. G., 2005, *AJ*, 130, 936
- Véron-Cetty M.-P., Véron P., 2010, *A&A*, 518, A10
- Visnovsky K. L., Impey C. D., Foltz C. B., Hewett P. C., Weymann R. J., Morris S. L., 1992, *ApJ*, 391, 560
- Wadadekar Y., 2004, *A&A*, 416, 35
- Whittle M., Wilson A. S., 2004, *AJ*, 127, 606
- Wrobel J. M., 1984, *ApJ*, 284, 531
- Xu C., Livio M., Baum S., 1999, *AJ*, 118, 1169
- Yun M. S., Reddy N. A., Condon J. J., 2001, *ApJ*, 554, 803

APPENDIX A: FIRST AND NVSS OBSERVED PARAMETERS FOR OUR SAMPLE LLAGN

Table A1 lists the FIRST and NVSS parameters for the first 10 sources of our sample.

This paper has been typeset from a \LaTeX file prepared by the author.

Table A1. FIRST and NVSS counterpart parameters of Seyfert and LINER galaxies

| VV10 parameters | | | | | FIRST parameters | | | | NVSS parameters | | | | | | |
|-----------------|-----------|-------|-------------|----------------|---------------------------|---------------------------|---|-------------|--|---------------------------|---|-------------|---|--------------------|-------------------------|
| RA | Dec | z | AGN type | M _v | S _p (mJy/b) | S _{int} (mJy) | size (max.× min.) (arcsec ²) | PA (deg) | R _{off} ^{FIRST} (″) | S _{int} (mJy) | size (max.× min.) (arcsec ²) | PA (deg) | R _{off} ^{NVSS} (″) | θ _{FIRST} | θ _{NVSS–FIRST} |
| (1) | (2) | (3) | (4) | (5) | (6) | (7) | (8) | (9) | (10) | (11) | (12) | (13) | (14) | (15) | (16) |
| 00 02 49.1 | +00 45 04 | 0.087 | S1 | 18.23 | 2.36 | 2.36 | 6.26 × 5.44 | 19.3 | 0.7 | 2.36 | 45.01 × 45.01 | 19.8 | 9.2 | 1.00 | 1.00 |
| 00 03 10.1 | +04 44 55 | 0.058 | S2 | 17.00 | 5.52 | 5.52 | 6.23 × 5.37 | 175.7 | 1.7 | 6.09 | 51.39 × 45.75 | 154.8 | 1.3 | 1.00 | 1.07 |
| 00 03 18.2 | +00 48 44 | 0.139 | S2 | 19.48 | 3.66 | 3.71 | 6.45 × 5.43 | 13.6 | 0.4 | 3.66 | 58.50 × 45.97 | 32.9 | 6.7 | 1.01 | 1.00 |
| 00 03 51.9 | -01 01 42 | 0.269 | S2 | 19.92 | 8.45 | 12.31 | 8.76 × 5.74 | 178.1 | 1.7 | 12.56 | 48.73 × 45.01 | 168.4 | 3.5 | 1.21 | 1.01 |
| 00 04 58.6 | +11 42 04 | 0.074 | S2 | 17.00 | 13.14 | 13.90 | 6.59 × 5.55 | 172.6 | 2.5 | 30.26 | 46.63 × 45.99 | -81.9 | 0.4 | 1.03 | 1.48 |
| 00 06 28.5 | -03 42 57 | 0.021 | S3 | 13.90 | 2.37 | 2.55 | 6.17 × 6.02 | 179.1 | 2.2 | 2.55 | 58.17 × 46.91 | -2.7 | 8.9 | 1.04 | 1.00 |
| 00 09 08.0 | +14 27 55 | 0.040 | S2 | 15.31 | 8.60 | 8.69 | 6.35 × 5.50 | 178.8 | 1.6 | 11.01 | 47.48 × 46.36 | 80.9 | 1.5 | 1.01 | 1.13 |
| 00 09 11.5 | -00 36 55 | 0.073 | S2 | 18.27 | 38.94 | 39.67 | 6.47 × 5.44 | 1.2 | 1.6 | 39.67 | 46.78 × 46.48 | -52.1 | 1.9 | 1.01 | 1.00 |
| 00 12 26.8 | -00 48 19 | 0.073 | S1 | 18.16 | 5.03 | 5.30 | 6.72 × 5.42 | 176.4 | 0.7 | 5.30 | 55.72 × 48.59 | -173.1 | 6.4 | 1.03 | 1.00 |
| 00 19 38.9 | -09 40 26 | 0.085 | S3 | 15.90 | 3.11 | 3.11 | 5.84 × 5.10 | 17.3 | 0.8 | 4.29 | 46.76 × 45.01 | -63.2 | 2.6 | 1.00 | 1.27 |
| 00 20 34.7 | -00 28 14 | 0.072 | S2 | 18.85 | 9.44 | 9.53 | 6.50 × 5.37 | 171.1 | 0.6 | 10.22 | 50.78 × 45.29 | 27.2 | 2.3 | 1.01 | 1.04 |

Notes: First 10 entries of our cross-matched catalog of VV10 and FIRST and NVSS for our sample of Seyfert and LINER galaxies.

Columns (1) - (2) : RA and DEC of the optical positions from VV10 catalog; Column (3) : redshift (z); Column (4) : Seyfert type *i.e.*, Seyfert type 1s, type 2s and LINERs are designated as S1, S2 and S3, respectively. Column (5) : observed B-band optical magnitude; Column (6) : FIRST peak flux density (S_p) in mJy; Column (7) : FIRST integrated flux density in mJy; Column (8) : FIRST fitted source size in arcsec; Column (9) : Position angle of FIRST source; Column (10) : Offset of FIRST counterpart from optical position (in arcsec); Column (11) : NVSS total flux density in mJy; Column (12) : NVSS fitted source size; Column (13) : Position angle of NVSS source; Column (14) : Offset of NVSS position from optical position; Column (15) : $\theta_{\text{FIRST}} = (S_{\text{int, FIRST}}/S_{\text{peak, FIRST}})^{1/2}$; Column (16) : $\theta_{\text{NVSS–FIRST}} = (S_{\text{int, NVSS}}/S_{\text{int, FIRST}})^{1/2}$.